Journal of Hazardous Materials 213–214 (2012) 7–18

Contents lists available at SciVerse ScienceDirect

Journal of Hazardous Materials

journal homepage: www.elsevier.com/locate/jhazmat

Biogenic hydroxyapatite (Apatite II^{TM}) dissolution kinetics and metal removal from acid mine drainage

J. Oliva[a], J. Cama[b,*], J.L. Cortina[c], C. Ayora[b], J. De Pablo[c]

[a] Department of Mining Engineering and Natural Resources, Politechnical University of Catalunya, Bases de Manresa 61-73, Manresa 08242, Catalonia, Spain
[b] Department of Geosciences, Institute of Environmental Assessment and Water Research, IDAEA, CSIC, Jordi Girona 18-26, Barcelona 08034, Catalonia, Spain
[c] Department of Chemical Engineering, Politechnical University of Catalunya, Avinguda Diagonal 647, Barcelona 08028, Catalonia, Spain

ARTICLE INFO

Article history:
Received 13 July 2011
Received in revised form 9 January 2012
Accepted 9 January 2012
Available online 28 January 2012

Keywords:
Apatite
Dissolution kinetics
Metal precipitation
AMD
PRB

ABSTRACT

Apatite II^{TM} is a biogenic hydroxyapatite (expressed as $Ca_5(PO_4)OH$) derived from fish bone. Using grains of Apatite II^{TM} with a fraction size between 250 and 500 μm, batch and flow-through experiments were carried out to (1) determine the solubility constant for the dissolution reaction

$$Ca_5(PO_4)_3(OH) \Leftrightarrow 5Ca^{2+} + 3PO_4^{3-} + OH^-,$$

(2) obtain steady-state dissolution rates over the pH range between 2.22 and 7.14, and (3) study the Apatite II^{TM}'s mechanisms to remove Pb^{2+}, Zn^{2+}, Mn^{2+}, and Cu^{2+} from metal polluted water as it dissolves.

The $\log K_S$ value obtained was -50.8 ± 0.82 at 25 °C. Far-from-equilibrium fish-bone hydroxyapatite dissolution rates decrease by increasing pH. Assuming that the dissolution reaction is controlled by fast adsorption of a proton on a specific surface site that dominates through the pH range studied, probably ≡P—O$^-$, followed by a slow hydrolysis step, the dissolution rate dependence is expressed in mol m^{-2} s^{-1} as

$$\text{Rate}_{25\,^\circ C} = -8.9 \times 10^{-10} \times \frac{9.96 \times 10^5 \times a_{H^+}}{1 + 9.96 \times 10^5 \times a_{H^+}}$$

where a_{H^+} is the proton activity in solution.

Removal of Pb^{2+}, Zn^{2+}, Mn^{2+} and Cu^{2+} was by formation of phosphate-metal compounds on the Apatite II^{TM} substrate, whereas removal of Cd^{2+} was by surface adsorption. Increase in pH enhanced the removal of aqueous heavy metals. Using the kinetic parameters obtained (e.g., dissolution rate and pH-rate dependence law), reactive transport simulations reproduced the experimental variation of pH and concentrations of Ca, P and toxic divalent metal in a column experiment filled with Apatite II^{TM} that was designed to simulate the Apatite II^{TM}–metal polluted water interaction.

1. Introduction

Natural and synthetic apatite minerals are powerful candidates for the remediation of metal-contaminated soils and groundwaters [1]. Apatite's capacity to form phosphate-metal compounds as it dissolves makes it a low cost candidate to fill permeable reactive barriers (PRBs) designed for remediation of metal contaminated soils and groundwaters. In particular, biogenic hydroxyapatite ($Ca_5(PO_4)_3(OH)$) (cowbone apatite and fish-bone apatite (e.g., Apatite II^{TM})) were investigated to assess their degree of effectiveness to sequester aqueous metals in polluted waters and contaminated soils among other type of materials [2,3]. Apatite II^{TM} proved to be the most efficient candidate, and more effective than cowbone apatite, due to its intrinsic properties (e.g., poor crystallinity and lack of structural fluorine). Conca and Wright et al. [4] treated acid mine drainage in a shallow alluvial groundwater containing elevated levels of Zn, Pb, Cd, Cu, SO_4 and NO_3 at the Success Mine tailings/waste rock pile (Idaho, USA) employing Apatite II^{TM} in a subsurface permeable reactive barrier (PRB). They showed that Apatite II^{TM} in the emplaced PRB was able to reduce the concentrations of Cd and Pb to below detection limit and reduced Zn to near background in the region. Also Apatite II^{TM} buffered the water pH to between 6.5 and 7 from an influent pH about 4.5. Recently, Oliva et al. [5,6] used Apatite II^{TM} in column experiments to study its removal capacity of some divalent cations (Fe(II), Zn(II), Mn(II) and Pb(II)) at acid pH range (3–5.6), emulating large scale passivation systems. The authors show that the efficiency of Apatite II^{TM} increases by decreasing water acidity.

* Corresponding author. Tel.: +34 934095410; fax: +34 934095410.
E-mail address: jordi.cama@idaea.csic.es (J. Cama).

0304-3894/$ – see front matter © 2012 Elsevier B.V. All rights reserved.
doi:10.1016/j.jhazmat.2012.01.027

Previous experiments were performed with natural, synthetic crystalline and biogenic apatite. Although the capacity for contaminated water remediation of Apatite II^{TM} is well proved, its solubility and reactivity have not been quantitatively assessed. This information is essential to design field scale treatment systems (e.g., passive permeable barriers with selected size/durability of apatite, thickness of the barrier, residence time in the barrier, etc.) to decontaminate metal polluted waters as is the case of acid mine drainage (AMD) with a significant metal content and acidity.

The aim of the paper is triple fold: (1) to measure the solubility of the Apatite II^{TM} and compare it with different apatites' solubility that can be found in the literature, (2) to investigate the hydroxyapatite (Apatite II^{TM}) dissolution kinetics and its pH-dependence reactivity of biogenic in the pH range between 2 and 7, and (3) to investigate the mechanisms of divalent metal removal by Apatite II^{TM} (Pb, Zn, Mn, Cd and Cu). The kinetic and solubility data obtained are applied to the reactive transport simulation of a column experiment of Apatite II dissolution and Cu retention. The results should improve the knowledge of hydroxyapatite kinetics and overall process of removing undesired cations from acid waters by using suitable water treatments (e.g., PRB.)

1.1. Previous studies

With respect to the solubility product of the synthetic apatite dissolution reaction

$$Ca_5(PO_4)_3(OH) \Leftrightarrow 5Ca^{2+} + 3PO_4^{3-} + OH^-, \quad (1)$$

Valsami-Jones et al. [7] obtained a value of $\log K_{s0} = -58 \pm 1$ at 25 °C. Rakovan [8] compiled a complete list of hydroxyapatite solubility products ($\log K_{s0}$) from literature that ranged from −55.9 to −88.5 between 20 and 30 °C, selecting a value of $\log K_{s0}$ of −57.5 as appropriate for stoichiometrically pure, well-crystallized hydroxyapatite. The dissolution kinetics of inorganic hydroxyapatite has not been intensively studied in the literature. Smith et al. [9] observed incongruent dissolution of hydroxyapatite in the pH region of 4.5–6.5 by means of batch experiments no longer than 24 h. Smith et al. [10] fitted their experimental data with an exponential restriction function related to the surface defect sites of the crystal. Christoffersen et al. [11] studied the kinetics of dissolution of pure calcium hydroxyapatite between pH 6.6 and 7 at 25 °C by means of rotating disc and found the dissolution rate to be pH dependent as $(H^+)^{0.57}$. Hull and Hull [12] fitted the same experimental data of Smith et al. [10] with a geometric model for incorporating the effects of hydroxyapatite surface irregularities (kinks and etch pits). Dorozhkin [13] studied the surface reaction of hydroxyapatite dissolution to propose a sequence of ionic detachment from the surface of apatite to solution. More recently, apatite dissolution rate was found to increase as pH decreases [7,14–16], yielding rates that were found to be proportional $(a_{H^+})^{0.6}$ at pH from 1 to 6. With respect to the mechanisms of metal retention Chen et al. [17] studied the pH effect on Pb, Zn and Cd sorption on hydroxyapatite carrying out batch experiments. The sorption of aqueous heavy metals was through a process of apatite dissolution followed by the precipitation of Pb, Cd and Zn bearing phases depending on the operating pH. Ma et al. [18] studied the effects of some aqueous metal on Pb immobilization by synthetic hydroxyapatite by conducting batch experiments for 2 h. Mavropoulos et al. [19] also used synthetic hydroxyapatite to study Pb adsorption showing that hydroxypyromorphite crystallites are continuously dissolved and recrystallized producing crystals with lower Ca content. Fuller et al. [20] showed that aqueous uranium is removed via surface sorption in the bone char apatite instead of precipitation. Due to sorption reversibility the use of bone apatite for uranium remediation was considered limited. Recently, hydroxyapatite capacity to remove Co [1,21], Cd, Pb and Zn [22], Pb [23], U(VI) [24] and Cu [25–27] has also been studied. The authors show that immobilization of metals mostly occurs via surface complexation and ion exchange with Ca^{2+}. Also, 3D-macroporous biopolymer-coated hydroxyapatite foams have been developed as potential devices for the treatment of Pb, Cd and Cu contamination of consumable waters [28].

2. Experimental methodology

2.1. Sample characterization

The Apatite II^{TM} raw sample was supplied by PIMS NW, Inc. This is biogenically precipitated apatite material that is derived from fish bones and has the general composition $Ca_{10-x}Na_x(PO_4)_{6-x}(CO_3)_x(OH)_2$, where $x < 1$, along with 30–40% by weight of associated organic materials in the internal porosity of the inorganic structure [4]. For the flow-through experiments, the sample was milled to size fraction between 250 and 500 μm. XRD patterns showed that the raw material mainly consists of hydroxyapatite and that calcite could be present up to ca. 5%. The specific surface area of the apatite sample was measured using the 5-point BET (N_2) method. Sample degassing lasted 2 h approximately at 140 °C. The BET surface area of raw Apatite II^{TM} (250 < fraction size < 500 μm) was $1.75 \pm 10\%$ m^2 g^{-1}. The final BET surface areas of some recovered samples after finishing the experiments ranged from 30 to 100 m^2 g^{-1}. SEM microphotographs show that the sample consisted of single pieces of hydroxyapatite with different elongated shapes and morphology (Fig. 1). The surface of the fragments varied from smooth to rough surfaces. Some fine microparticles appeared attached onto the surfaces of the large pieces. For the column experiments, the size fraction ranged between 500 and 3000 μm, and most of grain size distribution (90%) was below 1500 μm, one tenth of the column diameter (1.5 cm). HR-TEM images of Apatite II^{TM} were shown by [4].

2.2. Experimental set up and solution analysis

The batch experiments were conducted at 25 °C and initial pH values of 3 and 5; 2 g of Apatite II^{TM} were mixed into 1 L of 10^{-3} and 10^{-5} M $NaClO_4$ solutions, respectively. During the experiments, the mixture was permanently stirred by a magnetic bar. Spikes of 5 mL solution were extracted and analyzed for pH, Ca and P.

The flow-through experiments were carried out in a cell and experimental set-up similar to those described by Cama et al. [29]. Experimental runs were controlled by daily measurement of output pH. For the metal-free input solutions, those solutions were prepared by diluting a 1 M HCl source solution with double de-ionized water. The desired ionic strength in the initial solution (usually 0.01 N) was obtained by adding suitable amounts of NaCl or $NaClO_4$. Two experiments were conducted under buffer pH conditions by means of dipotassium hydrogen phthalate solution (MERCK) and adding different amounts of HCl (pH 4) or NaOH (pH 5). In the input solutions containing one heavy metal, the metal concentration was around 0.003 M: Pb was prepared from nitrate salt and HNO_3 matrix solution; Zn and Mn were prepared from the chloride salt and HCl matrix solution, and Cd and Cu were prepared from sulphate salts and H_2SO_4 matrix solutions. pH of input solutions ranged from 2 to 9. Two input multicomponent solutions were prepared. One that contained Pb, Mn and Zn was prepared with the respective metal-nitrate salt and the second one containing Cd and Cu was prepared with sulphate salts. Initial concentration of all cations was around 0.003 M. Nitric and sulphate acids were used to obtain an initial pH of ∼5.5.

One column experiment was conducted in a column of 2.5 cm length and 0.75 cm radius filled with 2.5 g of Apatite II. Solution was

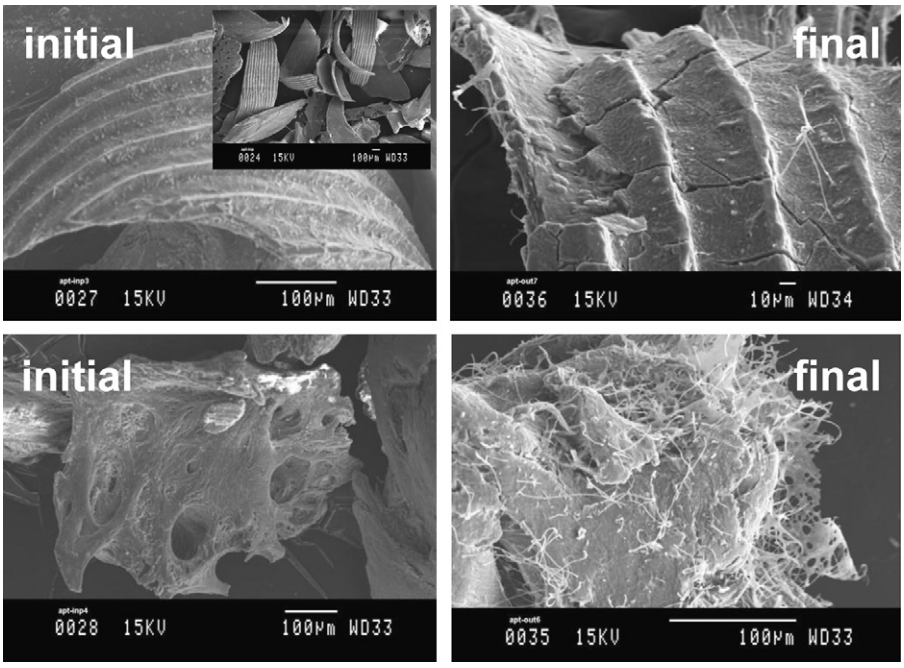

Fig. 1. SEM microphotographs of some of the particles of the initial sample and final samples before were totally dissolved.

administrated continuously through Teflon tubing connected to a peristaltic pump keeping a constant flow rate of 0.0 2 mL min^{-1}. Initial solution pH was 5.1 with Cu concentration of 1.2×10^{-3} M.

Total Ca, P, Pb, Zn, Mn, Cd and Cu input and output concentrations were analyzed by ICP-AES. The uncertainty in the measured concentrations was ±3% and the detection limit 5 μM. The pH was measured at experimental temperature on an unstirred aliquot of solution using a Ross combination electrode with a reported accuracy of ±0.02 pH units (±4.5% in H^+ activities). The pH electrode was standardized against commercialized pH buffer solutions Crison©.

3. Calculations

3.1. Dissolution rate

The dissolution rate in a mixed flow-through experiment, considering that the output solution composition is the same as the solution in the reactor cell, and that the steady state is reached, can be obtained by the difference between input and output solutions as

$$\nu_j R = -\frac{q}{A}(C_{j,\text{out}} - C_{j,\text{inp}}) \quad (2)$$

where $C_{j,\text{inp}}$ and $C_{j,\text{out}}$ are the concentrations of component j in the input and the output solutions, respectively (mol m^{-3}), t is time (s), V is the volume of the cell (m^3), A is the reactive surface area (m^2), q is the volume flow rate of the fluid through the system (m^3 s^{-1}) and ν_j is the stoichiometry coefficient of j in the dissolution reaction. Note that in our formalism, the rate is considered to be negative because it supposes a loss of material.

The error in the calculated rate (ΔR) is estimated according to the Gaussian error propagation method [30]. The error in the calculated rate was approximately 15% and is dominated by the uncertainty of the BET surface area measurement (±10%).

The hydroxyapatite dissolution reaction is expressed as Eq. (1) for which $\log K_s$ is calculated according to the mass action law as

$$K_s = \frac{\gamma_{Ca}^5 c_{Ca^{2+}}^5 \gamma_{PO_4^{3-}}^3 c_{PO_4^{3-}}^3}{\gamma_{OH^-} c_{OH^-}} \quad (3)$$

where γ_i and c_i represent the activity coefficients and the respective total concentrations. The activity coefficients are calculated with the PHREEQC code [31] and the MINTEQ database [32]. Concentrations are obtained from the batch experiments when the equilibrium was reached. Then the K_s value found was introduced in the code database, and the saturation index (SI) as follows

$$\text{SI} = \log \frac{\text{IAP}}{K_s} \quad (4)$$

where IAP is the ionic activity product of the solution. A negative, zero or positive SI value indicates undersaturation, equilibrium or precipitation, respectively.

4. Results and discussion

4.1. Apatite II™ solubility

The evolution of the batch experiment with pH 3 initial solution was characterized by a gradual increase of pH up to 6.3 (Fig. 2a), whereas in the experiment with pH 5 input solution the pH immediately raised to 7.6 (Fig. 2c). The release of Ca and P depended on pH evolution. In the first experiment the Ca and P were highly released at the onset of the experiment (Fig. 2b) and, in the latter, the Ca and P concentrations increased gradually (Fig. 2d). In the former experiment, the ratio Ca/P was 1.7, very close to the theoretical 1.66, probably due to microparticles dissolution from the beginning of the experiment. In the second experiment, the Ca/P was 1.5, being lower than the ideal 1.66. PHREEQC calculations showed that the solutions were undersaturated with respect to calcite in both experiments. Heterogeneity of the raw sample likely caused the different batch evolution observed with Ca concentration. After approximately 1000 h, phosphorus and calcium concentrations were considered to be in steady state and thus at equilibrium with respect to hydroxyapatite. Considering the respective average concentrations, values of $\log K_s$ were calculated according to Eq. (3), yielding $\log K_s$ of −50.2 and −51.4. The average $\log K_s$ value was -50.8 ± 0.8.

According to our results, Apatite II™ is more soluble than synthetic or natural apatites [7,8,33]. This is reasonable considering

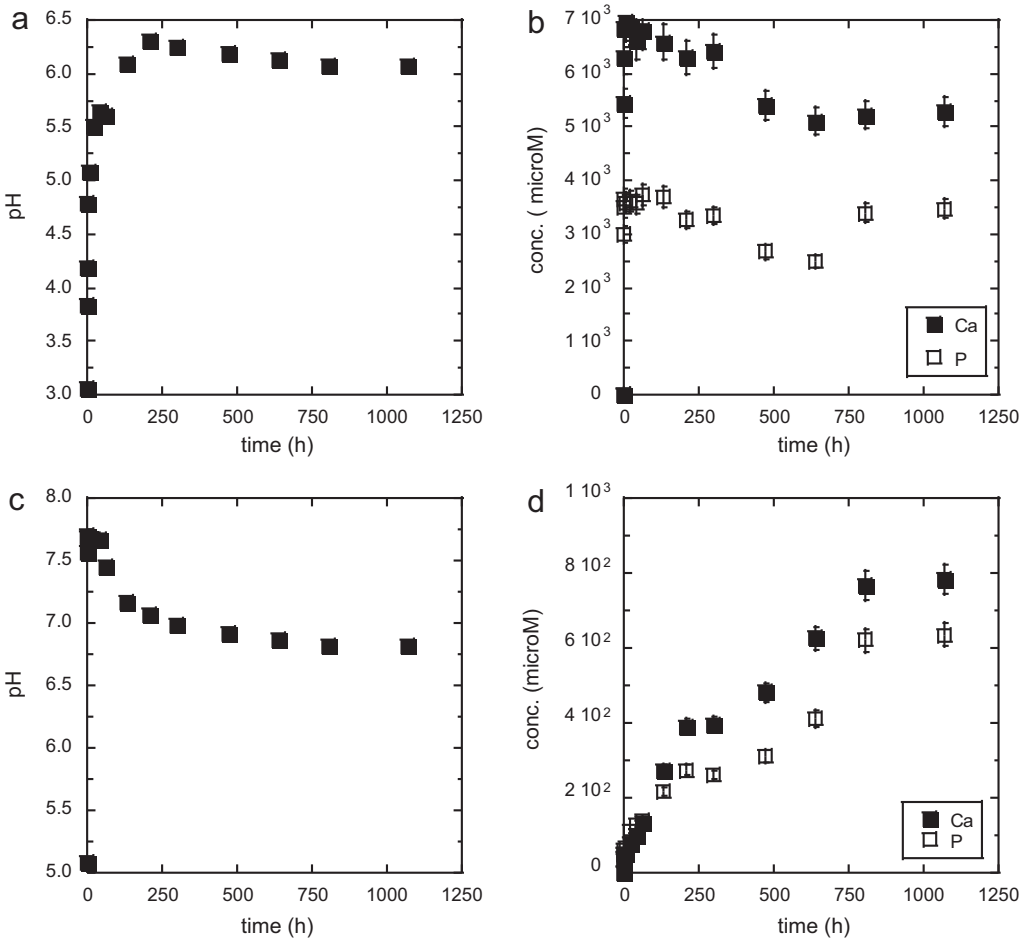

Fig. 2. Variation of concentrations of pH and Ca and P in the first batch experiment (initial pH 3) (a and b) and in the second batch experiment (initial pH 5) (c and d) as a function of time.

that Apatite II^{TM} shows a poorly to non-crystalline matrix with disperse thin nanocrystals [4]. Nonetheless, by means of batch experiments Zhu et al. [34] obtained the solubility of a synthetic crystalline hydroxyapatite yielding a mean log K_s of −53.28 at 25 °C. This value is closer to the one obtained in this study for Apatite II^{TM} than those previously reported for synthetic hydroxyapatite.

4.2. Apatite II^{TM} dissolution

Overall, the experiments conducted with acidic input solution showed similar behavior. On the onset of the experiment (less than 50 h) Ca and P were highly released to solution and pH increased (Fig. 3a). High concentrations of Ca and P were likely due to fast microparticles' dissolution, and the increase of pH was caused by the amount of hydroxyl released as hydroxyapatite (grains and microparticles) dissolved according to Eq. (1). Usually, after 100 h, Ca and P release and pH decreased to attain steady state (Fig. 3a and b). At this stage, dissolution rates of hydroxyapatite are calculated based on Ca and P release. Thereafter, output concentrations of Ca and P decreased to zero as sample kept on dissolving completely, and consequently pH decreased to the input pH solution. For the entire experimental run, the Ca/P stoichiometry ratio was close to 1.6. One experiment was stopped during steady-state stage to retrieve the solid sample. The XRD pattern showed that hydroxyapatite was still present. In the experiments carried out with basic input solution, pH decreased to about 7 (when input pH is 9) (Fig. 3c), and the initial dissolution of the sample was not very high (Fig. 3d). Thereafter, steady state was gradually approached. The Ca/P stoichiometric ratio gradually increased from 0.7 to 1.7 from the beginning to the steady-state stage. Initial non-stoichiometry was likely due to solution supersaturation with respect to hydroxyapatite as pH decreased from 9 to 7. Sample was not totally dissolved even after 400 h of experimental run. The experimental conditions and results are listed in Table 1.

Smith et al. [9] observed incongruent dissolution behavior associated to the hydroxyapatite initial state, while Christoffersen et al. [11] observed that the apatite dissolution was stoichiometric near neutral pH. Bengtsson et al. [35] showed that as hydroxyapatite dissolved a calcium-depleted layer relative to the bulk was formed, yielding a similar Ca/P ratio of 1.4 in solution (instead of 1.6). In this study, the dissolution of Apatite II^{TM} is stoichiometric within the analytical error, i.e., the Ca/P ratio is 1.6 ± 0.1 (Fig. 4).

4.3. Dissolution rates far-from-equilibrium

The observation that the dissolution rate remains constant throughout steady state, even though a significant amount of Apatite II^{TM} was dissolved (up to 40%), indicates that the (specific) reactive surface area did not decrease significantly during this stage. As in most of the experiments the solid sample run out, it was impossible to obtain the final surface area. Therefore, the dissolution rates are normalized to the initial specific surface area. Fig. 5 shows that the average dissolution rates decrease as pH increases from $-1.2 \pm 0.2 \times 10^{-9}$ at pH 2.2 to $-5.4 \pm 0.9 \times 10^{-11}$ mol m^{-2} s^{-1} at pH 7.1. The decrease in the dissolution rates as pH increases may be an effect of the increase of solution saturation state as

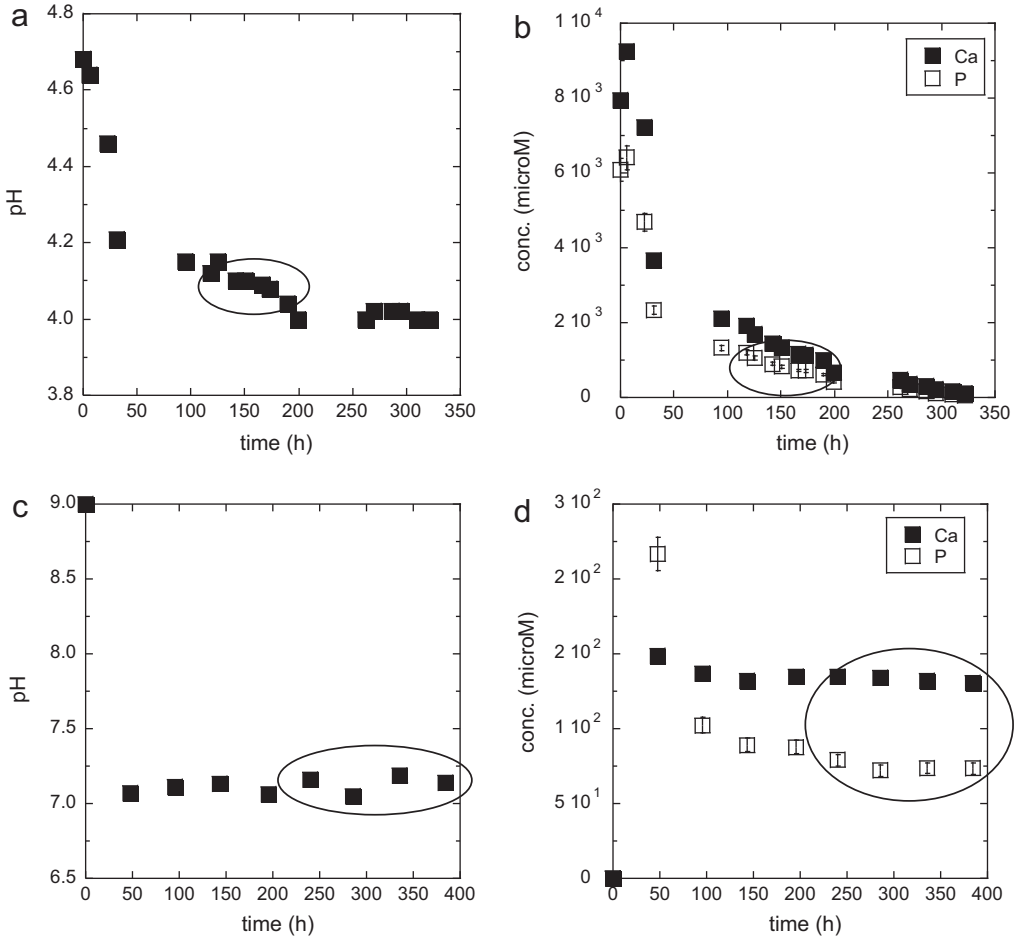

Fig. 3. Two representative flow-through experiments at 25 °C. With initial acid solution: variation of pH (a) and output concentrations of P and Ca (b) versus time. With circumneutral pH solution: variation of pH (c) and variation of output concentrations of Ca and P (d) versus time. Attainment of steady-state dissolution rates is denoted by the ellipses.

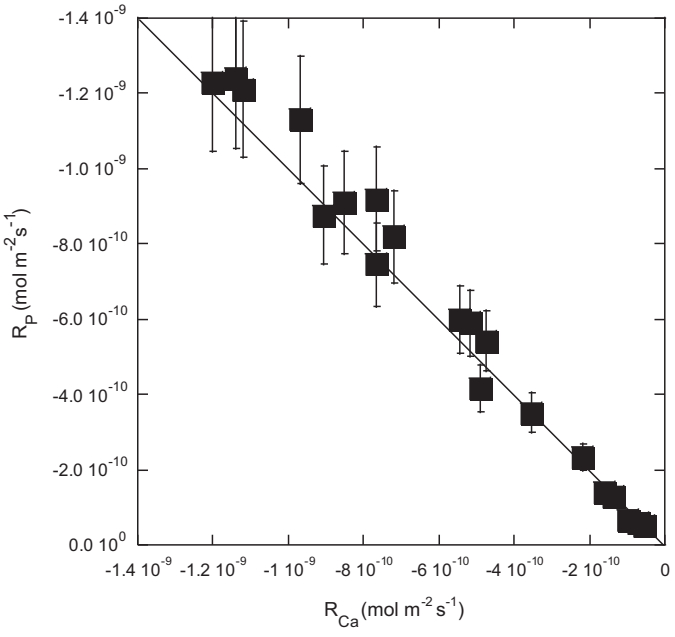

Fig. 4. Dissolution rate based on Ca and P released. Solid line denotes stoichiometric dissolution. Rates show the stoichiometry of the reaction.

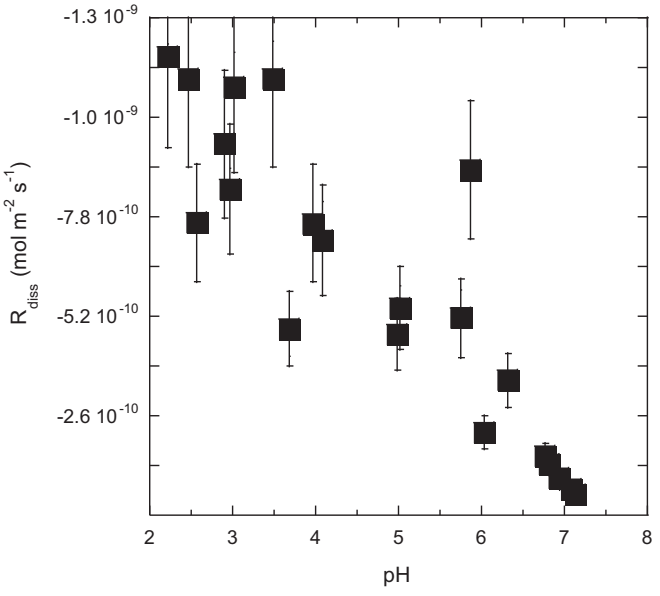

Fig. 5. Apatite II™ dissolution rates (R_{diss}) based on release of Ca and P versus pH at 25 °C. The rates mainly decrease at pH > 3.5.

Table 1
Experimental conditions in the flow-through experiments for Apatite II^{TM} dissolution.

Experiment	Time (h)	Flow rate (ml min^{-1})	pH initial	pH final	Ca (o) (μM)	P (o) (μM)	Ca/P	Initial mass (g)	St. st. mass (g)	BET surface (m^2 g^{-1})	Diss. rate (Ca) (mol m^{-2} s^{-1})	Diss. rate (P) (mol m^{-2} s^{-1})	log Rate$_{Ca}$ (mol m^{-2} s^{-1})	log Rate$_P$ (mol m^{-2} s^{-1})	log(R_{diss}) (mol m^{-2} s^{-1})	SI
1	1321	0.030	3.00	6.03	684.68	439.35	1.56	0.358	0.179	1.754	−2.2E−10	−2.3E−10	−9.7	−9.6	−9.65	−6.7
2	219	0.190	3.00	3.68	237.50	121.05	1.96	0.351	0.176	1.754	−4.9E−10	−4.2E−10	−9.3	−9.4	−9.35	−27.1
3	240	0.190	5.00	6.76	90.33	47.63	1.90	0.350	0.206	1.754	−1.6E−10	−1.4E−10	−9.8	−9.9	−9.83	−8.9
4	229	0.190	9.00	6.93	55.33	23.08	2.42	0.351	0.206	1.754	−9.7E−11	−6.7E−11	−10.0	−10.2	−10.09	−9.7
5	322	0.190	3.00	5.86	881.26	512.27	1.72	0.352	0.352	1.754	−9.0E−10	−8.8E−10	−9.0	−9.1	−9.05	−7.1
6	249	0.190	7.00	6.82	76.78	44.09	1.75	0.353	0.208	1.754	−1.3E−10	−1.3E−10	−9.9	−9.9	−9.88	−8.9
7	432	0.046	9.00	7.14	132.11	72.96	1.81	0.351	0.206	1.754	−5.6E−11	−5.1E−11	−10.3	−10.3	−10.27	−4.8
8	310	0.105	9.00	7.09	82.73	41.83	1.98	0.351	0.234	1.754	−7.1E−11	−6.0E−11	−10.2	−10.2	−10.19	−6.9
9	413	0.056	3.00	3.96	1481.57	867.23	1.71	0.351	0.206	1.754	−7.6E−10	−7.5E−10	−9.1	−9.1	−9.12	−18.6
10	411	0.084	2.03	2.22	1954.69	1193.30	1.64	0.355	0.261	1.754	−1.2E−09	−1.2E−09	−8.9	−8.9	−8.92	−29.8
11	171	0.079	2.89	6.31	709.37	424.27	1.67	0.352	0.303	1.754	−3.5E−10	−3.5E−10	−9.5	−9.5	−9.45	−4.7
12	293	0.083	2.65	5.75	950.08	631.62	1.50	0.356	0.290	1.754	−5.2E−10	−5.9E−10	−9.3	−9.2	−9.26	−7.4
13	294	0.083	2.13	2.46	1546.80	1070.72	1.44	0.351	0.215	1.754	−1.1E−09	−1.4E−09	−8.9	−8.8	−8.90	−28.8
14	427	0.083	2.26	2.57	1228.93	841.44	1.46	0.354	0.254	1.754	−7.6E−10	−9.2E−10	−9.1	−9.0	−9.08	−28.8
15	266	0.084	2.37	2.90	1537.67	1030.83	1.49	0.354	0.253	1.754	−9.7E−10	−1.1E−09	−9.0	−8.9	−8.98	−25.7
16	247	0.083	2.45	3.02	1582.18	992.83	1.59	0.353	0.223	1.754	−1.1E−09	−1.2E−09	−9.0	−8.9	−8.93	−24.9
17	195	0.084	2.45	6.36	2203.40	1367.66	1.61	0.401	0.259	1.754	−1.1E−09	−1.2E−09	−8.9	−8.9	−8.92	−21.1
18	195	0.084	2.45	2.97	1304.15	809.51	1.61	0.401	0.243	1.754	−8.5E−10	−9.1E−10	−9.1	−9.0	−9.06	−25.9
19	335	0.073	4.03	4.08	1203.96	749.82	1.61	0.501	0.231	1.754	−7.2E−10	−8.2E−10	−9.1	−9.1	−9.11	−18.4
20	426	0.077	4.97	5.02	1060.92	671.50	1.58	0.502	0.406	1.754	−5.4E−10	−6.0E−10	−9.3	−9.2	−9.24	−12.2
21	430	0.072	5.00	4.99	588.34	365.65	1.61	0.35	0.17	1.754	−4.7E−10	−5.4E−10	−9.3	−9.3	−9.29	−14.5

St. st. means steady state. log γ_i to obtain SI are calculated with PHREEQC [31]. SI is calculated according to Eq. (1) for which $IAP_{eq} = 1.26 \times 10^{22}$.

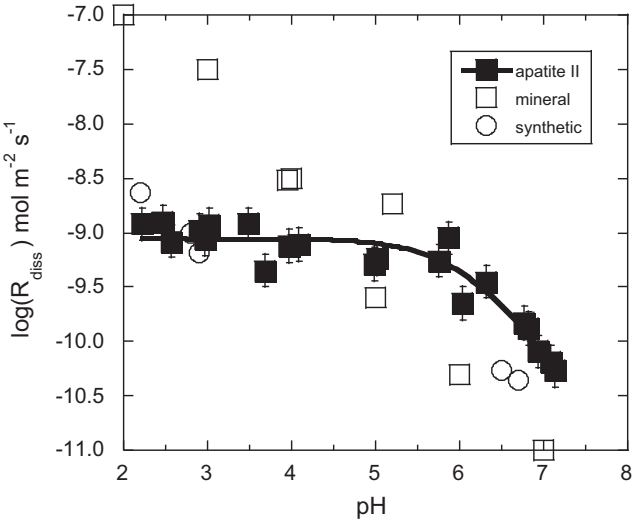

Fig. 6. Log R_{diss} versus pH at 25 °C. The solid line represents the best fit using Eq. (10). Open symbols correspond to dissolution rates of natural apatite (squares) and synthetic apatite (circles) according to [6,13,14].

pH increases (approach to the close-to-equilibrium condition) instead of a truly pH catalytic effect. All the steady-state dissolution rates were obtained at undersaturation with respect to Apatite II^{TM} as the SI values indicate (Table 1). Experiments conducted at pH very close to 7 (pH nearly constant) are adequate to separate the possible effect of solution saturation state from that of pH on the dissolution rate. The steady-state dissolution rate values of these experiments (Table 1) are the same within error ($-5.9 \times 10^{-11} \pm 0.8$ mol m^{-2} s^{-1}) and the respective SI values range from −4.8 to −9.7. It appears thus that the dissolution rate is constant and independent of SI (the dissolution plateau [36], i.e., the dissolution rate is obtained at far-from-equilibrium conditions where Ca varies from 55.33 to 132.11 μM and P from 23.08 to 72.96 μM. Therefore, dissolution rate values obtained at SI values lower than −4.8 correspond to far-from-equilibrium dissolution rates. Therefore, the steady-state dissolution rates of Apatite II^{TM} are obtained at far from equilibrium conditions. Consequently the increase of dissolution rate as pH decreases is due to a pH catalytic effect. Fig. 6 plots log rate with pH. It is observed that from pH 2.2 to 4.5 the dissolution rate appears to be constant while at pH >4.5 the dissolution rate decreases. The solid line is the best fitting based on a Langmuir isotherm as explained below.

Dissolution rates of mineral and synthetic apatite obtained in previous studies [7,14,15] are also plotted in mol m^{-2} s^{-1} in Fig. 6. It is observed that dissolution rates of natural apatite are faster than both synthetic and Apatite II^{TM}. Valsami et al. [7] argue that higher surface roughness and probable chemical heterogeneity was responsible for the higher dissolution rate of natural apatite. The dissolution rate of Apatite II^{TM} is comparable to the one of synthetic apatite in the pH range from 2 to 3 and slightly faster at near neutral pH. Under very acidic pH conditions, the apatite dissolution rate is very fast, and probably the degree of crystallinity and the crystal defects do not determine the dissolution mechanism. In the mildly acidic pH where dissolution rates are slower, the dissolution rate of Apatite II^{TM} is slightly faster than that of synthetic apatite likely due to the poorest crystallinity, the existence of crystal defects and amorphous material.

4.4. Dissolution rate-pH dependence

It is assumed that (1) Apatite II^{TM} (or hydroxyapatite) dissolution rate under acidic conditions is controlled by a reaction path

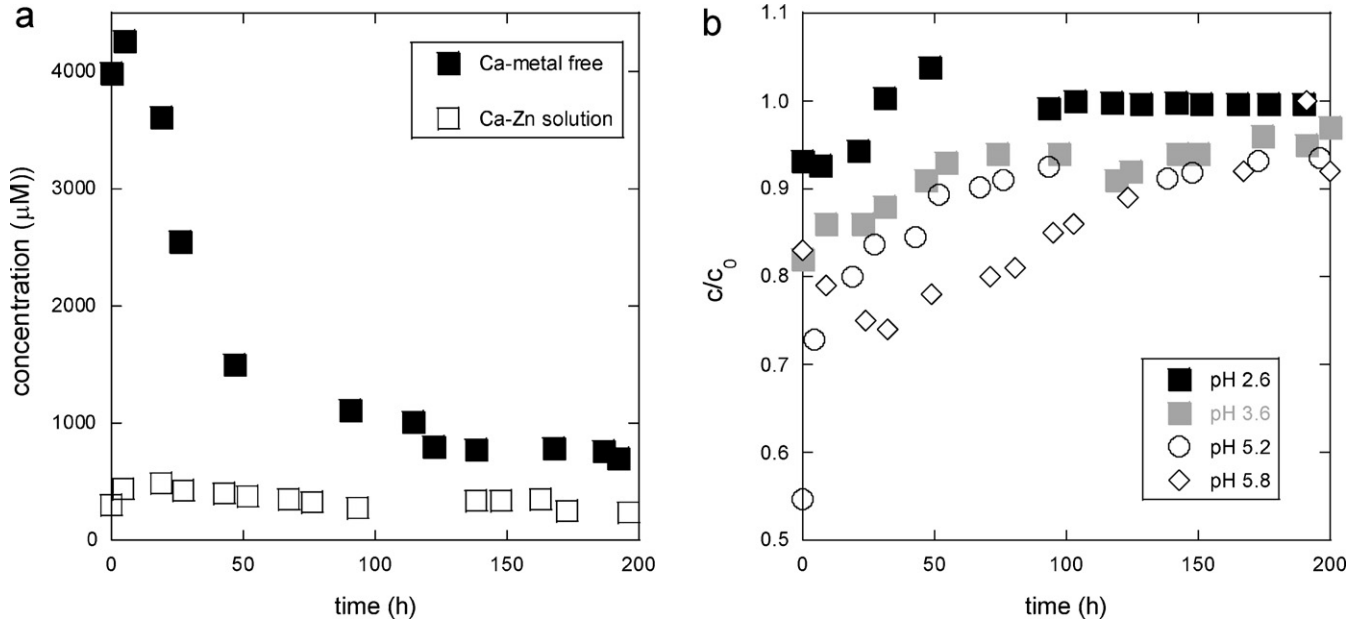

Fig. 7. Single Zn solution in a metal-removal experiment. (a) Variation of concentration of Ca with time in one representative flow-through experiment at 25 °C and pH 5.5 that is compared to Ca released in similar metal-free dissolution experiment. (b) Variation of the Zn relative concentration with time in the Zn-removal experiments. As pH is increased the removed amount of Zn increases.

that consists of fast adsorption of a proton on a specific surface site followed by a slow hydrolysis step and that (2) the adsorption of the protons on this surface site may be described by a simple independent Langmuir adsorption isotherm:

$$X_{\mathrm{i,ads}} = F_{\mathrm{i}} \frac{b_{\mathrm{i}} \times C_{\mathrm{i}}}{1 + (b_{\mathrm{i}} \times C_{\mathrm{i}})} \tag{5}$$

where *F*i is the maximum surface coverage of protons on site i, *b*i is a constant related to the energy of adsorption on site i and a_{H^+} is the activity of protons in the solution.

In the following discussion the letters S_1 and S_2 represent two surface sites. The combination S_i—*M* represents a metal on the surface. Adsorption of a proton on a surface site close to the metal would influence the bond strength and thus affect the dissolution rate. Each proton promoted reaction path consists of adsorption of a proton on the mineral surface followed by a proton-mediated hydrolysis step. The rate-determining step is the breakdown of the S_i—*M* bond:

$$S_i\text{–}M + \mathrm{H}^+ \overset{\text{fast}}{\longleftrightarrow} \mathrm{H}^+\text{–}S_i\text{–}M \overset{\text{fast}}{\underset{k_i}{\longrightarrow}} S_i + M + \mathrm{H}^+ \tag{6}$$

If steady-state conditions are maintained, the rate of this reaction path, R_{i} is [37]:

$$\frac{R_{\mathrm{i}}}{\rho_{\mathrm{r}}} = k_{\mathrm{i}} \cdot X_{\mathrm{i,ads}} \tag{7}$$

where $k_i\,(\mathrm{s}^{-1})$ is the rate coefficient of this path, $\rho_{\mathrm{r}}\,(\mathrm{mole\,m}^{-2})$ is the density of reactive surface sites on the mineral surface and $X_{\mathrm{i,ads}}$ is the molar fraction of the surface site that is protonated. Substituting the Langmuir adsorption isotherm (Eq. (5)) into Eq. (7), gives

$$\frac{R}{\rho_{\mathrm{r}}} = k \cdot F \frac{b \times a_{\mathrm{H}^+}}{1 + (b \times a_{\mathrm{H}^+})} \tag{8}$$

or

$$R = k' \cdot F \frac{b \times a_{\mathrm{H}^+}}{1 + (b \times a_{\mathrm{H}^+})} \tag{9}$$

where $k' = k{\cdot}F{\cdot}\rho_{\mathrm{r}}$ and *b* were calculated from a non-linear regression of Eq. (9) using least squares. The black solid line in Fig. 6 is the best-fit curve based on Eq. (10) that is described by:

$$R = -8.9^{-10} \cdot \frac{9.96 \times 10^5 \times a_{\mathrm{H}^+}}{1 + (9.96 \times 10^5 \times a_{\mathrm{H}^+})} \quad R^2 = 0.95 \tag{10}$$

The rate of hydroxyapatite dissolution consists of fast adsorption of a proton on a surface site followed by a slow hydrolysis step. One active site controls the rate under acidic conditions, e.g., ≡PO^- [38]. The pH at the point of zero charge, $\mathrm{pH_{pzc}}$, has been found to vary from 4.35 to 7.6 for hydroxyapatite [38]. For fluor-apatite the $\mathrm{pH_{pzc}}$ has been found to be 7.13 for a CO_2 atmosphere.

4.5. Divalent-metal removal and Apatite II™ dissolution

Removal of aqueous divalent metals as apatite dissolved showed similar behavior. As a representative case, Fig. 7a shows the variation of calcium released in a Zn-removal experiment with time as Apatite II™ dissolved at pH 5.2 and compares with the calcium release as apatite dissolved in a metal-free solution and similar pH. Ca variation in the presence of aqueous Zn was lower than in the metal-free solution. Another observation was that the Ca/P ratio was higher than the stoichiometric one, being indicative of a deficit of aqueous phosphor. Similar behavior was observed in the removal of Pb, Mn and Cu (Table 2). Fig. 7b shows the variation of Zn relative concentration with respect to initial concentration with time. It is observed that removal of Zn lasted longer and increased as pH increased. Likewise the Ca/P ratio increased with pH. Similar metal removal and P deficit was observed in the Pb, Mn and Cu removal-experiments. PHREEQC calculations showed that apatite dissolved in undersaturated solutions with respect to apatite and in supersaturated solutions with respect to divalent metal-phosphate phases (Table 2). Also, their SI increased with pH. The newly formed phosphate phases were observed by SEM (Fig. 8) and identified by XRD (Fig. 9). The XRD patterns and SEM images of the reacted Apatite II™ powder showed the presence of hopeite ($Zn_3(PO_4)_2{\cdot}4H_2O$), pyromorphite ($Pb_5(PO_4)_3OH$), and switzerite ($Mn_3(PO_4)_2{\cdot}7H_2O$) and their amount on the Apatite II™ substrate increased by increasing pH. Regarding Cu removal, the aqueous

Table 2
Experimental conditions in the flow-through experiments for metal removal and SI calculated using the MINTEQ database [32].

Expt.	Electrolyte	Anion inp. (μM)	Metal out. (μM)	Flow rate ($mL\,min^{-1}$)	pH	Ca/P	Ca output (μM)	P output (μM)	Mass (g)	R_{diss} ($mol\,m^{-2}\,s^{-1}$)	$\log R_{diss}$ ($mol\,m^{-2}\,s^{-1}$)	SI				
												Hydroxyapatite	$CdSO_{4x}\cdot H_2O$	$Cd_3(PO_4)_2$	Gypsum	Otavite
Cd-1	$CdSO_4$	3609	3460	0.076	2.0	1.7	1138	660	0.216	7.3E−10	−9.1	−27.3	−4.1	−14.0	−1.4	−5.2
Cd-2	$CdSO_4$	3276	3475	0.075	4.5	1.7	977	591	0.302	4.7E−10	−9.3	−9.2	−3.9	−3.4	−1.2	−0.2
Cd-3	$CdSO_4$	3340	3276	0.076	5.9	5.7	281	49	0.327	1.3E−10	−9.9	−5.4	−3.4	−0.04	−1.8	2.4
Cd-4	$CdSO_4$	3279	2943	0.047	5.7	3.1	294	95	0.337	7.8E−11	−10.1	−5.8	−3.9	**−0.4**	−1.7	**2.0**

Expt.	Electrolyte	Anion inp. (μM)	Metal out. (μM)	Flow rate ($mL\,min^{-1}$)	pH	Ca/P	Ca output (μM)	P output (μM)	Mass (g)	R_{diss} ($mol\,m^{-2}\,s^{-1}$)	$\log R_{diss}$ ($mol\,m^{-2}\,s^{-1}$)	SI						
												Hydroxyapatite	$CuSO_4$	$Cu_3(PO_4)_2$	Gypsum	$CuCO_3$	Antlerite	Brochantite
Cu-1	$CuSO_4$	3473	3440	0.065	2.1	1.6	2400	1520	0.174	1.8E−09	−8.7	−23.8	−8.8	−10.2	−1.0	−9.1	−11.2	−16.8
Cu-2	$CuSO_4$	3610	3154	0.067	4.0	1.8	1037	581	0.280	4.4E−10	−9.4	−12.6	−8.6	−1.2	−1.2	−5.3	−3.5	−5.3
Cu-3	$CuSO_4$	3341	3134	0.073	5.0	4.6	313	69	0.325	1.3E−10	−9.9	−10.9	−8.6	**1.0**	−1.7	−3.4	**0.6**	**0.7**
Cu-4	$CuSO_4$	3280	2617	0.050	4.9	1.1	407	369	0.331	1.2E−10	−9.9	−8.8	−8.7	**1.9**	−1.6	−3.6	**−0.1**	**−0.2**

Expt.	Electrolyte	Anion inp. (μM)	Metal out. (μM)	Flow rate ($mL\,min^{-1}$)	pH	Ca/P	Ca output (μM)	P output (μM)	Mass (g)	R_{diss} ($mol\,m^{-2}\,s^{-1}$)	$\log R_{diss}$ ($mol\,m^{-2}\,s^{-1}$)	SI				
												Hydroxyapatite	$Ni_3(PO_4)_2$	Calcite	$NiCO_3$	$Ni(OH)_2$
Ni-1	$Ni(NO_3)_2$	3239	3250	0.068	2.7	1.7	778	468	0.293	3.4E−10	−9.5	−22.4	−12.0	−9.6	−10.6	−8.1
Ni-2	$Ni(NO_3)_2$	3323	3300	0.072	3.9	1.8	355	201	0.329	1.4E−10	−9.9	−16.5	−7.7	−7.5	−8.2	−5.7
Ni-3	$Ni(NO_3)_2$	3288	3229	0.074	6.5	3.6	143	39	0.350	2.7E−11	−10.6	−2.6	**1.1**	−3.5	−3.8	**−0.5**
Ni-4	$Ni(NO_3)_2$	3128	3029	0.038	6.6	2.9	125	44	0.351	1.5E−11	−10.8	−2.0	**1.4**	−3.5	−3.8	**−0.3**

Expt.	Electrolyte	Anion inp. (μM)	Metal out. (μM)	Flow rate ($mL\,min^{-1}$)	pH	Ca/P	Ca output (μM)	P output (μM)	Mass (g)	R_{diss} ($mol\,m^{-2}\,s^{-1}$)	$\log R_{diss}$ ($mol\,m^{-2}\,s^{-1}$)	SI				
												Hydroxyapatite	$MnHPO_4$	$Mn_3(PO_4)_2$	Calcite	Rhodochrosite
Mn-1	$MnCl_2$	3135	3472	0.074	2.7	1.9	833	439	0.310	3.8E−10	−9.4	−22.4	**2.4**	−19.4	−9.6	−7.0
Mn-2	$MnCl_2$	3245	3200	0.075	3.7	2.2	264	119	0.341	9.8E−11	−10.0	−19.2	**2.9**	−16.4	−8.0	−5.0
Mn-3	$MnCl_2$	3292	3185	0.086	5.8	12.5	137	11	0.347	6.4E−11	−10.2	−7.3	**4.5**	−9.0	−4.2	−1.0
Mn-4	$MnCl_2$	3142	2697	0.038	6.4	9.9	402	41	0.350	8.2E−11	−10.1	−3.4	**5.0**	−6.9	−2.8	−0.1

Expt.	Electrolyte	Anion inp. (μM)	Metal out. (μM)	Flow rate ($mL\,min^{-1}$)	pH	Ca/P	Ca output (μM)	P output (μM)	Mass (g)	R_{diss} ($mol\,m^{-2}\,s^{-1}$)	$\log R_{diss}$ ($mol\,m^{-2}\,s^{-1}$)	SI			
												Hydroxyapatite	Calcite	Cerrusite	$Pb(OH)_2$
Pb-1	$Pb(NO_3)_2$	3274	2534	0.086	2.7	6.2	1268	336	0.212	1.7E−09	−8.8	−25.2	−12.2	−4.4	−5.5
Pb-2	$Pb(NO_3)_2$	3496	2576	0.089	3.4	83.1	764	9	0.287	4.5E−10	−9.3	−26.0	−8.2	−3.0	−4.1
Pb-3	$Pb(NO_3)_2$	3364	3111	0.088	5.0	6.1	215	35	0.333	1.1E−10	−10.0	−15.8	−5.6	**0.2**	−0.8
Pb-4	$Pb(NO_3)_2$	3158	2590	0.039	5.5	218	441	2	0.341	9.6E−11	−10.0	−14.4	−4.4	**1.1**	**0.1**

Expt.	Electrolyte	Anion inp. (μM)	Metal out. (μM)	Flow rate ($mL\,min^{-1}$)	pH	Ca/P	Ca output (μM)	P output (μM)	Mass (g)	R_{diss} ($mol\,m^{-2}\,s^{-1}$)	$\log R_{diss}$ ($mol\,m^{-2}\,s^{-1}$)	SI			
												Hydroxyapatite	$Zn_3(PO_4)_2\cdot 4H2O$	Calcite	Smithsonite
Zn-1	$ZnCl_2$	3390	3300	0.083	2.6	1.6	588	368	0.319	3.1E−10	−9.5	−24.1	−11.9	−9.9	−7.6
Zn-2	$ZnCl_2$	3434	3215	0.088	3.6	2.8	399	144	0.330	2.0E−10	−9.7	−18.8	−8.4	−8.1	−5.6
Zn-3	$ZnCl_2$	3261	3015	0.090	5.2	27.3	280	10	0.329	1.5E−10	−9.8	−11.7	−4.4	−5.1	−2.5
Zn-4	$ZnCl_2$	2630	2343	0.036	5.8	15.5	338	22	0.344	6.7E−11	−10.2	−6.1	−1.6	−3.9	−1.5

SI calculations are based on MINTEQ database [32]. Hydroxyapatite is $Ca_5(PO_4)_3OH$. SI values in bold indicate precipitation of the phase indicated.

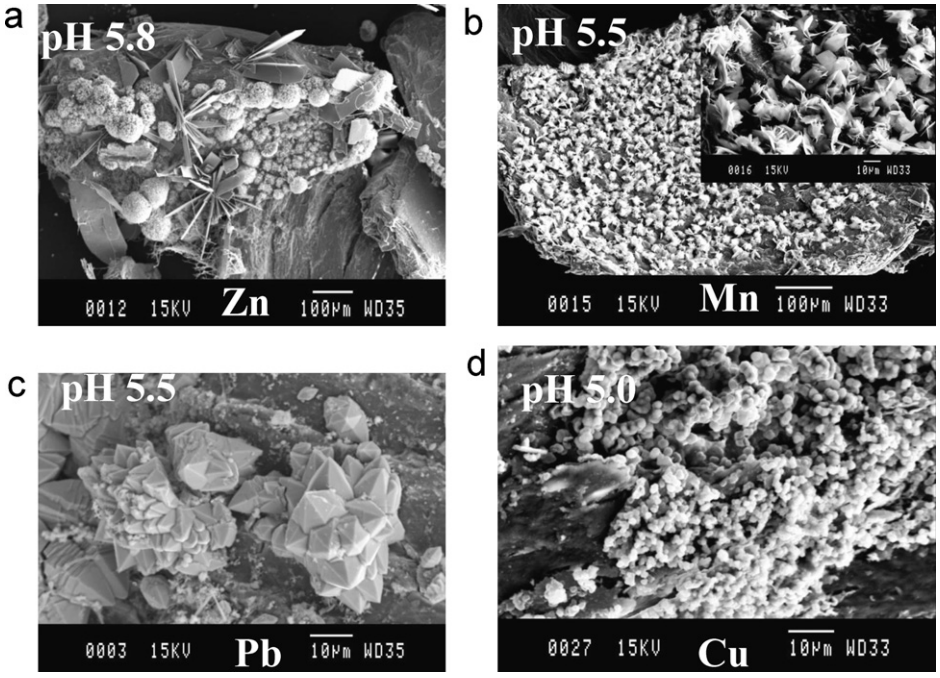

Fig. 8. SEM microphotographs that show the metal-phosphates formed in the metal removal experiments: (a) hopeite, (b) switzerite over Apatite II™ substrate (the insert shows in detail some of the switzerite crystals), (c) pyromorphite and (d) Cu-bearing precipitate.

species Cu^{2+} and $CuSO_4$ were predominating over the pH range studied. However, a Cu-amorphous precipitate was observed on the apatite substrate (Fig. 8d). Cd removal was observed although no Cd-phosphate precipitates were detected on the Apatite II™ substrate.

Based on the Ca released during the metal removal, apparent apatite dissolution rates were computed. Fig. 10 depicts the variation of log apparent rate with pH to show that Apatite II™ dissolution decreased with the removal of divalent cations (empty symbols). This fact is due to loss of reactive surface of Apatite II™ as it dissolved and the metal-bearing phosphates precipitated. It is therefore suggested that some surficial phosphate molecules promoted the formation of new phosphate phases acting as phosphate seeds to capture divalent cations. In the meantime some other phosphate was released to solution as well as calcium. Therefore metal-phosphate formation depends on accessible surface of Apatite II™. In fact, the experiments lasted 225 h, and metal-phosphate precipitates did not passivate Apatite II™ surface and prevent its dissolution.

In the multicomponent solution experiments conducted to remove Pb, Mn and Zn it was observed that only pyromorphite formed with precipitates of lower crystallinity than of those formed in unicomponent Pb-solution (Fig. 11a). EDX analyses confirmed the mere existence of Pb. In the columns designed to remove Cu and Cd, spheric and planar precipitates were observed (Fig. 11b). EDX analyses showed the existence of Cu and Cd in the new precipitates.

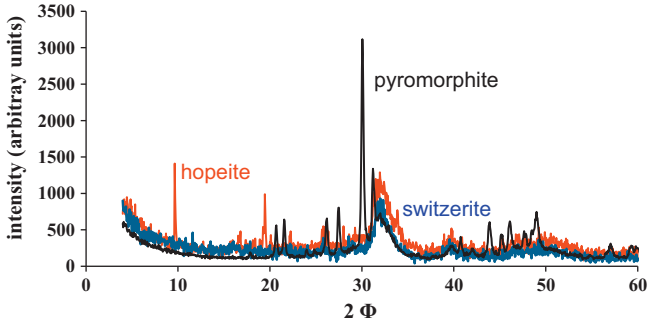

Fig. 9. XRD patterns that show the presence of hopeite ($Zn_3(PO_4)_2{\cdot}4H_2O$), pyromorphite ($Pb_5(PO_4)_3OH$) and switzerite ($Mn_3(PO_4)_2{\cdot}7H_2O$).

4.6. Column experiment: Apatite II™ dissolution and Cu removal

The apatite II dissolution rate law has been used to simulate the observed behavior of apatite dissolution and Cu removal in the column experiment. The column experiment showed complete Cu retention. Fig. 12 shows the advancement of the Cu front along the column with time. After 86 d Cu precipitates had been formed all over the column with no further Cu removal. Fig. 13 shows the variation of concentration of Ca, P and Cu and pH variation. It is observed that as Apatite II™ dissolved (high release of Ca and P) pH increased to approx. 8.3. At this stage the injected Cu concentration (1.2×10^{-3} M) was totally depleted. Thereafter, as concentration of

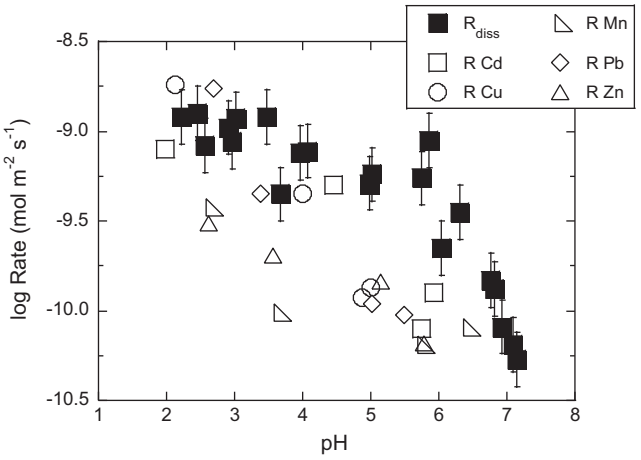

Fig. 10. Log R_{diss} and log apparent dissolution rates versus pH at 25 °C. The latter rates are lower than the rates in metal free solutions (Log R_{diss}) indicating the loss of apatite reactivity as metal-phosphates precipitate.

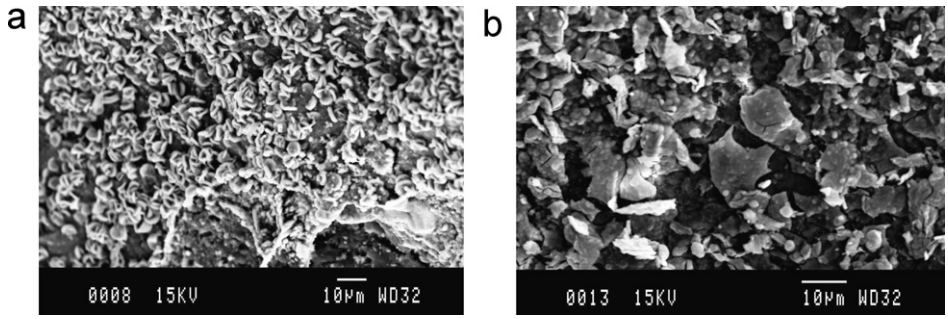

Fig. 11. SEM microphotographs of the retrieved samples in multicomponent-solution experiments: (a) precipitate of pyromorphite in the Pb–Zn–Mn solution (pH 5.5) and (b) Cu-precipitates in the Cu–Cd solution (pH 5.5).

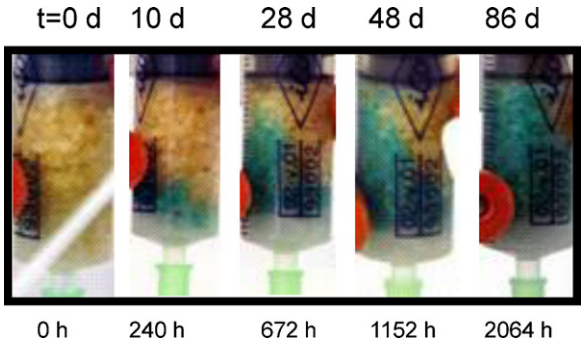

Fig. 12. Retained Cu in the column experiment. The length of the column and the radius are 2.5 and 0.75 cm, respectively. The Cu front advances along the column with time. After 86 d (2064 h) Cu is not removed.

Ca and P diminished together with pH (down to initial pH of 4.9), Cu concentration started to increase up to its initial value. Hence, after ca. 2000 h Apatite II^{TM} exhaustion started preventing Cu retention.

Simulations using the dissolution rates and the expression to account for the pH-rate dependence found in the present study fitted the experimental data in the columns (Fig. 13). Solid lines representing concentration of Ca, P and Cu and pH mimicked the experimental behavior in the columns. Based on the aqueous evolution in this column experiment and considering that a PRB thickness is 1 m, filled with Apatite II^{TM} (e.g., porosity of 40%) with acidic water (pH of 5) circulating through (e.g., flow rate of 1 $m^3\ m^{-2}\ d^{-1}$), total Cu removal is predicted to last approx. 30 a. Likewise, apatite II^{TM} capacity to remove Cu in the same PRB but in extreme conditions where water pH might be as low as 3 (e.g., in AMD) is predicted to last 15 a (Fig. 14). Notice that at this solution pH, Cu-precipitates are released back to solution after apatite consumption (ca. 1000 h). These calculations help foresee the PRB design and future maintenance.

It is shown that with the obtained experimental data normalized to units that allow further upscaling (e.g., pore volumes, mass of reactive and residence time) it is possible to upscale from the laboratory to the field by means of the reactive transport numerical simulation. This procedure would allow predictions of the system behavior prior to field-test performance. Also, the small residence time in the experiment was suitable to reproduce cementation and clogging. However, no cementation was observed because the reactive material was exhausted before clogging could occur. Reactive transport calculations showed that precipitated Cu-phases did not clog porosity before consumption of apatite II. It is possible that hydraulic properties (e.g., permeability) may change from laboratory to field scale. Nonetheless, if permeability changes, which

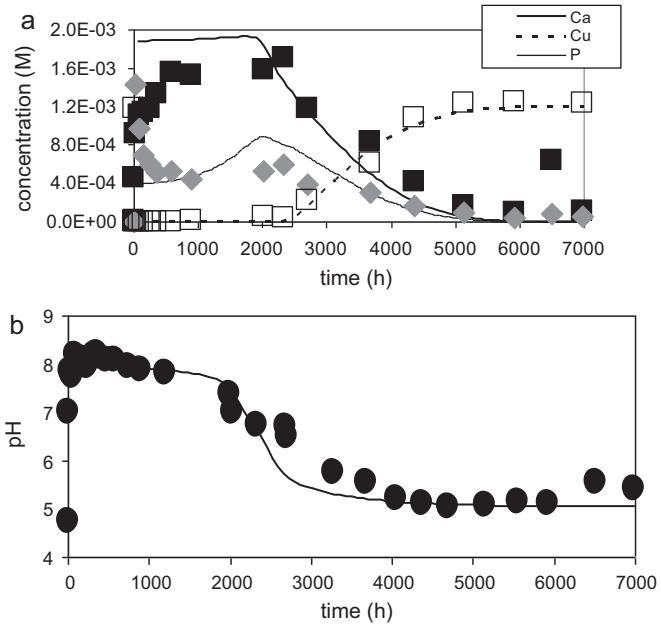

Fig. 13. (a) Variation of Ca (black solid square), P (grey solid rhombus) and Cu (empty square) versus time in the Cu-column experiment. Lines denote the simulation results. Total Cu removal occurred up to 2100 h. (b) pH variation with time. Solid line denotes the simulated pH. The initial concentration of Cu and pH of 1.2×10^{-3} M and 4.9, respectively.

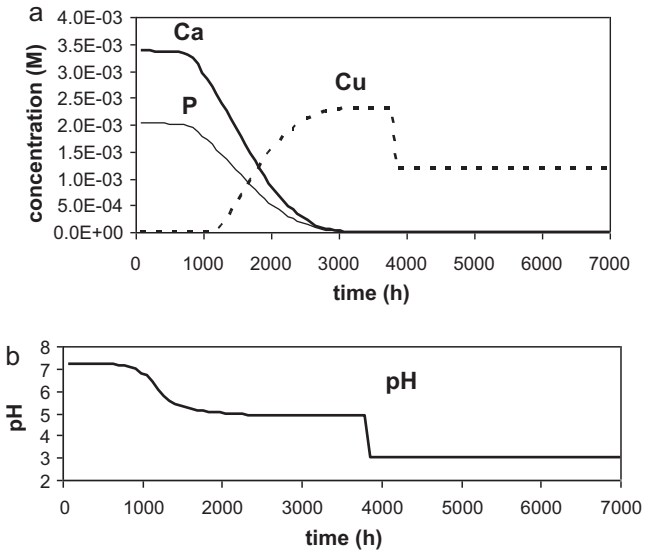

Fig. 14. Simulated variation of Ca, P and Cu (a) and pH (b) versus time in a similar Cu-column experiment with initial concentration of Cu and pH of 1.2×10^{-3} M and 3, respectively. In this case, Cu is totally removed until 1100 h, and retained Cu is released back to solution.

tends to increase with scale [39], resulting in an improvement of PRB performances. According to a previous work on passive treatment systems [40], field PRB performs slightly better than expected from column experiments [41].

5. Conclusions

Biogenic Apatite II^{TM} solubility ($\log K = -50.8 \pm 0.8$ at 25 °C) is higher than those of inorganic (natural and synthetic) hydroxyapatite reported in the literature ($\log K = -57.5$ at 25 °C).

Dissolution experiments allowed confirmation of the Apatite II^{TM} dissolution stoichiometry (Ca/P ratio = 1.6) and calculation of steady-state Apatite II^{TM} dissolution rates at far-from-equilibrium conditions ($-4.8 < SI < -29.8$). Apatite dissolution was pH independent at pH ≤ 5 and decreased at pH > 5, allowing formulation of the rate-pH dependence according to a Langmuir type isotherm. The observed pH-rate variation shows that Apatite II^{TM} dissolution is lower than other apatites' dissolution, suggesting a long durability in acid waters.

Metal removal occurred via metal-phosphate precipitation with Pb, Zn, Mn and Cu. Cd removal occurred although a Cd-phosphate phase was not identified. Metal precipitation was favored by increasing pH as solution supersaturation with respect to the metal-phosphates increased. Metal removal was, however, dependent on apatite's reactive surface. In the presence of several cations, Pb was removed by pyromorphite formation and no Mn and Zn were removed. When Cu and Cd were together the former was mostly removed. Therefore, competition to form metal-phosphates among these cations is to be taken into account to remediate mine waters.

Kinetic parameters obtained in the study were used to appropriately simulate the Cu removal in a column experiment using the RETRASO code [42]. Therefore, simulations would allow reliable estimations of Apatite II^{TM} durability as backfill material in passive reactive barriers. It was shown that very acidic pH diminishes considerably the reactive time of Apatite II^{TM} material in the treatment system.

Acknowledgments

Along the course of the study we have received the technical support of Sergi Sanllorente, Javier Pérez and Vanessa Ouro. Scientific comments with Araceli Garrido improved the quality of the paper. We thank Rafel Bartrolí and Toni Padró for their technical assistance in the ICP-AES analysis. SEM inspection and BET measurement were conducted at Scientific-Technical Services of Barcelona University. This work has been possible thanks to financial support of the CICYT project # CTM2007-66724-C02. The authors would like to thank the thoughtful reviews from three anonymous reviewers.

References

[1] I. Smiciklas, A. Onjia, S. Raicevic, D. Janackovic, M. Mitric, Factors influencing the removal of divalent cations by hydroxyapatite, J. Hazard. Mater. 152 (2008) 876–884.
[2] J.L. Conca, Phosphate-Induced Metal Stabilization (PIMS). Final report to the US Environmental Protection Agency # 68D60023, 1997.
[3] S. Raicevic, J.V. Wright, V. Veljkovic, J.L. Conca, Theoretical stability assessment of uranyl phosphates and apatites: selection of amendments for in situ remediation of uranium, Sci. Total Environ. 355 (2006) 13–24.
[4] J.L. Conca, J. Wright, An Apatite II^{TM} permeable reactive barrier to remediate groundwater containing Zn, Pb and Cd, Appl. Geochem. 21 (2006) 1288–1300.
[5] J. Oliva, J. De Pablo, J.L. Cortina, J. Cama, C. Ayora, The use of Apatite II^{TM} to remove divalent metal ions zinc (II), lead (II), manganese (II) and iron (II) from water in passive treatment systems: column experiments, J. Hazard. Mater. 184 (2010) 364–374.
[6] J. Oliva, J. De Pablo, J.L. Cortina, J. Cama, C. Ayora, Removal of cadmium, copper, nickel, cobalt and mercury from water by Apatite II^{TM}: column experiments, J. Hazard. Mater. 194 (2011) 312–323.
[7] E. Valsami-Jones, K.V. Ragnarsdottir, A. Putnis, D. Bosbach, A.J. Kemp, G. Cressey, The dissolution of apatite in the presence of aqueous metal cations at pH 2–7, Chem. Geol. 151 (1998) 215–233.
[8] J. Rakovan, Growth and surface properties of apatite phosphates – geochemical, geobiological and materials importance, in: M.J. Kohn, J. Rakovan, J.M. Hughes (Eds.), Rev. Mineral. Geochem. 48 (2002) 51–86.
[9] A.N. Smith, A.M. Posner, J.P. Quirk, Incongruent dissolution and surface complexes of hydroxyapatite, J. Colloid Interface Sci. 48 (1974) 442–449.
[10] A.N. Smith, A.M. Posner, J.P. Quirk, A model describing the kinetics of dissolution of hydroxyapatite, J. Colloid Interface Sci. 62 (1977) 475–494.
[11] J. Christoffersen, M.R. Christoffersen, N. Kjaergaard, The kinetics of dissolution of calcium hydroxyapatite in water at constant pH, J. Cryst. Growth 43 (1978) 501–511.
[12] A.B. Hull, J.R. Hull, Geometric modeling of dissolution kinetics: application to apatite, Water Res. 23 (1987) 707–714.
[13] S. Dorozhkin, Surface reactions of apatite dissolution, J. Colloid Interface Sci. 191 (1997) 489–497.
[14] M.W. Guidry, F.T. Mackenzie, Experimental study of igneous and sedimentary apatite dissolution: control of pH, distance from equilibrium, and temperature on dissolution rate, Geochim. Cosmochim. Acta 67 (2003) 2949–2963.
[15] C. Chaïrat, J. Schott, E.H. Oelkers, J.-E. Lartigue, N. Harouiya, Kinetics and mechanism of natural fluorapatite dissolution at 25 C and pH from 3 to 12, Geochim. Cosmochim. Acta 71 (2007) 5901–5912.
[16] N. Harouiya, N.C. Chaïrat, S.J. Köhler, R. Gout, E.H. Oelkers, The dissolution kinetics and apparent solubility of natural apatite in batch reactors at temperatures from 5 to 50 °C and pH from 1 to 6, Chem. Geol. 244 (2007) 554–568.
[17] X. Chen, J.V. Wright, J.L. Conca, L.M. Peurrung, Effects of pH on heavy metal sorption on mineral apatite, Environ. Sci. Technol. 31 (1997) 624–631.
[18] Y.Q. Ma, S.J. Traina, T.J. Logan, J.A. Ryan, Effects of aqueous Al, Cd, Cu, Fe(II), Ni and Zn on Pb immobilization by hydroxyapatite, Environ. Sci. Technol. 28 (1994) 1219–1228.
[19] E. Mavropoulos, A.M. Rossi, A.M. Costa, C.A. Perez, J.C. Moreira, M. Saldanha, Studies on the mechanisms of lead immobilization by hydroxyapatite, Environ. Sci. Technol. 36 (2002) 1625–1629.
[20] C.C. Fuller, J.R. Bargar, J.A. Davis, Molecular-scale characterization of uranium sorption by bone apatite materials for a permeable reactive barrier demonstration, Environ. Sci. Technol. 37 (2003) 4642–4649.
[21] I.I. Smiciklas, S. Dimovic, I. Plecas, M. Mitric, Removal of Co^{2+} from aqueous solutions by hydroxyapatite, Water Res. 40 (2006) 2267–2274.
[22] I.R. Sneddon, M. Orueetxebarria, M.E. Hodson, P.F. Schofield, E. Valsami-Jones, Use of bone meal amendments to immobilise Pb, Zn and Cd in soil: a leaching column experiment, Environ. Pollut. 144 (2006) 816–825.
[23] S. Baillez, A. Nzihou, D. Bernache-Assolant, E. Champoin, P. Sharrock, Removal of aqueous lead ions by hydroxyapatites: equilibria and kinetic processes, J. Hazard. Mater. 139 (2007) 443–446.
[24] F.G. Simon, V. Biermann, C. Segebade, M. Hedrich, Behaviour of uranium in hydroxyapatite-bearing permeable reactive barriers: investigation using ^{237}U as a radioindicator, Sci. Total Environ. 326 (2004) 249–256.
[25] A. Corami, F. D'Acapito, S. Mignardi, C. Ferrini, Removal of Cu from aqueous solutions by synthetic hydroxyapatite: EXAFS investigation, Mater. Sci. Eng. B 149 (2008) 209–213.
[26] M. Sljivic, I. Smiciklas, I. Plecas, M. Mitric, The influence of equilibration conditions and hydroxyapatite physico-chemical properties onto retention of Cu^{2+} ions, Chem. Eng. J. 148 (2009) 80–89.
[27] Y.J. Wang, J.H. Chen, Y.X. Cui, S.Q. Wang, D.M. Zhou, Effects of low-molecular weight organic acids on Cu(II) adsorption onto hydroxyapatite nanoparticles, J. Hazard. Mater. 162 (2009) 1135–1140.
[28] M. Vila, S. Sanchez-Salcedo, M. Cicuendez, I. Izquierdo-barba, M. Vallet-Regí, Novel biopolymer-coated hydroxyapatite foams for removing heavy-metals from polluted water, J. Hazard. Mater. 192 (2011) 71–77.
[29] J. Cama, V. Metz, J. Ganor, The effect of pH and temperature on kaolinite dissolution rate under acidic conditions, Geochim. Cosmochim. Acta 66 (2002) 3913–3926.
[30] J. R. Barrante, Applied mathematics for Physical Chemistry, Prentice Hall Inc.
[31] D.L. Parkhurst, User guide to PHREEQC – a computer program for speciation, reaction-path, advective-transport, and inverse geochemical calculations. US Geological Survey Water Resources Investigation Report 95-4227, Lakewood, Colorado, 1995, 143 pp.
[32] J.D. Allison, D.S., Brown, K.J. Novo-Gradac, MINTEQA2/PRODEF2, A Geochemical Assessment Model for Environmental Systems: Version 3.0 User's Manual. EPA/600/3-91/021, Athens, GA, USA: EPA, 1991.
[33] A.S. Knox, D.I. Kaplan, M.H. Paller, Phosphate sources and their suitability for remediation of contaminated soils, Sci. Total Environ. 357 (2006) 271–279.
[34] Y. Zhu, X. Zhang, Y. Chen, Q. Xie, J. Lan, M. Qian, N. He, A comparative study on the dissolution and solubility of hydroxyapatite and fluorapatite at 25 °C and 45 °C, Chem. Geol. 268 (2009) 89–96.
[35] A. Bengtsson, A. Shchukarev, P. Persson, S. Sjöberg, A solubility and surface complexation study of a non-stoichiometric hydroxyapatite, Geochim. Cosmochim. Acta 73 (2009) 257–267.

[36] K.L. Nagy, A.E. Blum, A.C. Lasaga, Dissolution and precipitation of kaolinite at 80 °C and pH 3: the dependence on solution saturation state, Am. J. Sci. 291 (1991) 649–686.
[37] A.C. Lasaga, Rate laws of chemical reaction, in: A.C. Lasaga, R.J. Kirkpatrick (Eds.), Reviews in Mineralogy, 1981, pp. 1–67.
[38] L. Wu, W. Forsling, P.W. Schindler, Surface complexation of calcium minerals in aqueous solution. 1. Surface protonation at fluorapatite–water interfaces, J. Colloid Interface Sci. 147 (1991) 178–185.
[39] J. Guimerà, J. Carrera, A comparison of hydraulic and transport parameters measured in low-permeability fractured media, J. Contam. Hydrol. 41 (2000) 261–281.
[40] M.A. Caraballo, T.S. Rotting, F. Macías, J.M. Nieto, C. Ayora, Field multi-step limestone and MgO passive system to treat acid mine drainage with high metal concentrations, Appl. Geochem. 24 (2009) 2301–2311.
[41] T.S. Rotting, R.C. Thomas, C. Ayora, J. Carrera, Passive treatment of acid mine drainage with high metal concentrations using dispersed alkaline substrate, J. Environ. Qual. 37 (2008) 1741–1751.
[42] M.W. Saaltink, F. Batlle, C. Ayora, J. Carrera, S. Olivella, RETRASO, a code for modeling reactive transport in saturated and unsaturated porous media, Geol. Acta 2 (2004) 235–251.